Lorentz Mapping of Magnetic Fields in Hot, Dense Plasmas

Spontaneous generation of magnetic (***B***) fields occurs pervasively in galactic[1,2] and stellar[3] settings and in numerous laboratory plasma experiments.[2,4] For the case of the hot, dense plasmas of laser–plasma experiments[4,5] or for scaled astrophysics experiments in the laboratory,[2,4] self-generated magnetic and electric fields are often intertwined and inextricably coupled to the dynamics of the plasma evolution. This coupling makes the field-generation process complicated and also means that the effects of the fields can directly or indirectly act back on the plasma itself. Measuring local, self-generated fields, and distinguishing between electric (***E***) and magnetic fields, is a formidable task.[6]

This article describes a monoenergetic proton radiography method that, when used in combination with Lorentz force mapping, allows one to precisely measure plasma field strengths as well as unequivocally discriminate between electric and magnetic fields. Electromagnetic fields in a high-energy-density plasma can be measured by passing monoenergetic protons through the plasma and observing how their trajectories are deflected by the fields. Any trajectory bending is due to the Lorentz force

$$\boldsymbol{F} = q\left(\boldsymbol{E} + \frac{\boldsymbol{v} \times \boldsymbol{B}}{c}\right), \tag{1}$$

where q is the proton charge and $\boldsymbol{v}$ is the proton velocity, acting over a path length ℓ characteristic of the fields' spatial extent. For true quantitative analysis of data it is critical that $\boldsymbol{v}$ be known accurately. If it is known in advance whether a field is $\boldsymbol{B}$ or $\boldsymbol{E}$, Eq. (1) can be used directly to relate any observed trajectory bending to field strength. If bending is observed but there is no absolute knowledge of which field is present, the individual contributions of $\boldsymbol{E}$ and $\boldsymbol{B}$ can be determined by making two independent measurements. This discrimination can be accomplished by three methods, although practical implementation is often challenging: The first method measures the same plasma in the same way but with the direction of $\boldsymbol{v}$ reversed; the second measures the same plasma but with protons of two discrete values of $|\boldsymbol{v}|$; and the third measures two plasmas that are identical except for the reversal of any $\boldsymbol{B}$ field.

The experiment reported here utilized the third method to resolve ambiguities of field identity and field strength. The experimental setup used monoenergetic proton radiography, as illustrated in Fig. 119.12(a). A pulse of 14.9-MeV protons was generated from fusion reactions of deuterium (D) and helium-3 (^{3}He) in a D_2-^{3}He–filled, glass-shell capsule driven by 17 OMEGA[7] laser beams. This proton source was completely characterized using spectral,[8] spatial,[9] and temporal[10] diagnostics; it had a mean energy of 14.9±0.1 MeV, a spectral half-width <1.5% (or half-width in the proton velocity distribution <0.75%), an emission region FWHM of 45 μm, and a duration of 130 ps. The protons were used to image two identical, expanding plasma bubbles, formed on opposite sides of a 5-μm-thick plastic (CH) foil by two 1-ns-long laser interaction beams. Both beams had spot diameters of 850 μm and intensities of 8×10^{13} W/cm^2; they were fired simultaneously and incident at 23.5° from the normal to the foil. To break the nearly isotropic proton fluence into "beamlets" (~1000 protons each) whose deflections could easily be observed and quantified, 150-μm-period nickel meshes were placed on opposite sides of the foil. Figure 119.12(b) is the resulting radiograph, recorded on a CR-39 nuclear track detector,[8] with laser timing adjusted so that the bubbles were recorded 1.36 ns after the onset of the interaction beams.

The top bubble image in Fig. 119.12(b) is a type that we have recently begun studying[11,12] and contrasting to predictions of the 2-D radiation–hydrodynamic code LASNEX.[13] The simulations indicated that proton deflections are purely a result of a toroidal $\boldsymbol{B}$, parallel to the foil, arising from the $\nabla n_e \times \nabla T_e$ magnetic-field source term (where n_e and T_e are the electron number density and temperature).[14,15] While the data and simulations were qualitatively similar, there was a consistent, quantitative mismatch between them throughout the bubble evolution (predicted apparent bubble sizes were ~25% smaller than observed;[16,17] predicted field strengths were larger overall than observed; and field morphology details differed). This discrepancy effectively precluded use of the simulations to justify any *a priori* assumption that observed proton deflections were caused exclusively by a $\boldsymbol{B}$ field and not by any component $\boldsymbol{E}_{\parallel}$ (parallel to the foil) of an $\boldsymbol{E}$ field.

To provide direct experimental identification of the field type as well as strength, the current experiment was designed so the second bubble reversed the sign of any $\boldsymbol{B}$ relative to the first bubble (as seen from the detector) while leaving any $\boldsymbol{E}_{\parallel}$ unchanged. If the $\boldsymbol{B}$ reversal had no effect on deflections of the monoenergetic protons used to image the plasma, any deflections would necessarily have been dominated by $\boldsymbol{E}_{\parallel}$. If the reversal resulted in equal but oppositely directed deflections of the monoenergetic protons, it would demonstrate the clear dominance of $\boldsymbol{B}$. Qualitatively, the latter is what is seen in the image: the bubble on the front side of the foil (top of image) appears expanded, while the bubble on the back side appears contracted.

Figure 119.12(c) shows the absolute values of the beamlet deflection angles θ as a function of position at the foil; θ is calculated from the apparent displacement of a beamlet in an image relative to where it would be without deflection. The peak θ values occur at the foil on two circles of the same radius, and the amplitudes are the same for both circles. This is seen quantitatively in Fig. 119.13(a), which shows θ as a function of radius measured from each bubble's center. Because of Eq. (1) and the fact that $\boldsymbol{B}$ is reversed between the bubbles while $\boldsymbol{E}$ is not, it follows that we can decompose the total deflections $\theta_{\text{top}}(r)$ and $\theta_{\text{bottom}}(r)$ for the top and bottom bubbles into parts due only to $\boldsymbol{B}$ and $\boldsymbol{E}$ by assuming the two bubbles are otherwise equivalent. Then

$$\theta_{\text{top}}(r) = \theta_{\boldsymbol{E}}(r) + \theta_{\boldsymbol{B},\text{top}}(r), \qquad (2)$$

$$\theta_{\text{bottom}}(r) = \theta_{\boldsymbol{E}}(r) - \theta_{\boldsymbol{B},\text{top}}(r), \qquad (3)$$

from which it follows that

$$\theta_{\boldsymbol{E}}(r) = \left[\theta_{\text{top}}(r) + \theta_{\text{bottom}}(r)\right]/2, \qquad (4)$$

$$\theta_{\boldsymbol{B}}(r) = \left[\theta_{\text{top}}(r) - \theta_{\text{bottom}}(r)\right]/2. \qquad (5)$$

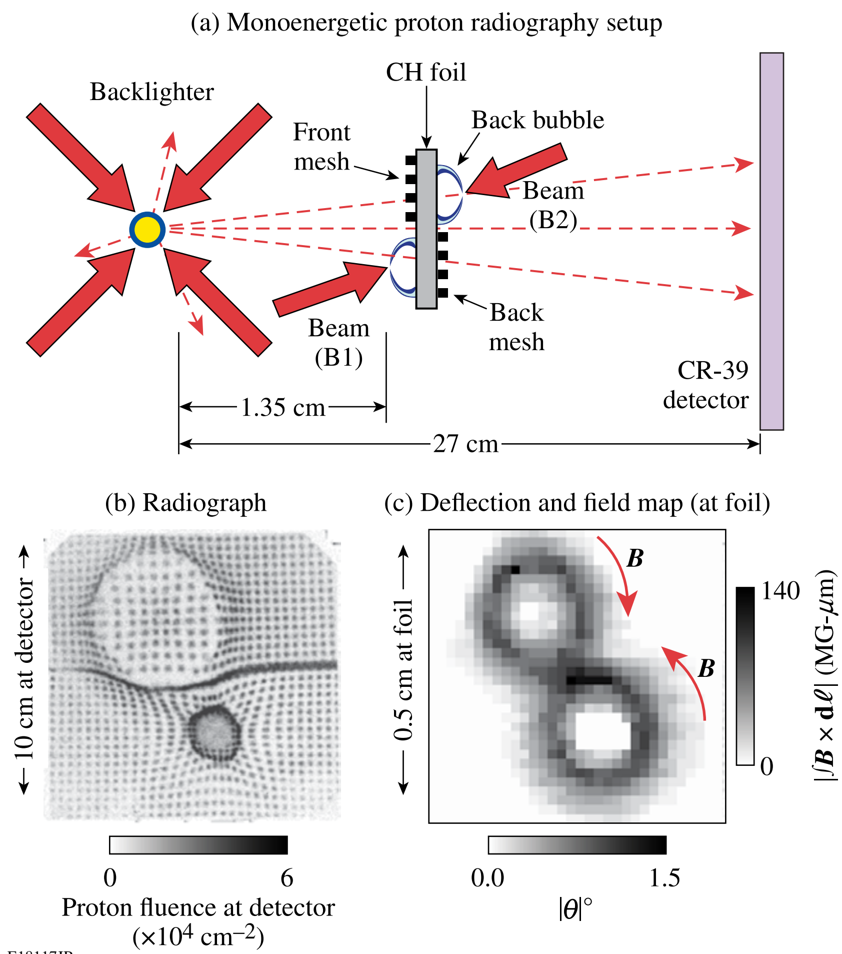

Figure 119.12
(a) Proton radiography setup, (b) proton radiograph of two laser-generated plasma bubbles, and (c) spatial map of proton beamlet deflection angle (or equivalently the magnetic field strength) as a function of position on the foil. Note in Fig. 119.13(b) that the deflections are associated almost exclusively with a $\boldsymbol{B}$ field near the foil, meaning that (c) can also be viewed as a magnetic field map. Part (c) shows that the two bubbles were actually the same size, even though the apparent sizes are different in the radiograph. Orientation of the images is as seen from behind the detector, looking toward the backlighter. The radiograph was acquired during OMEGA shot 46535.

The results are shown in Fig. 119.13(b) after converting $\theta_{\boldsymbol{B}}(r)$ and $\theta_{\boldsymbol{E}}(r)$ to $\int \boldsymbol{B} \times \mathbf{d}\boldsymbol{\ell}$ and $\int \boldsymbol{E}_{\parallel} \times \mathbf{d}\boldsymbol{\ell}$ using Eq. (1). The vertical display scales for $\boldsymbol{E}$ and $\boldsymbol{B}$ were selected so the relative amplitudes of the curves indicate the relative amounts of proton deflection. The effect of $\boldsymbol{B}$ greatly dominates the effect of $\boldsymbol{E}_{\parallel}$, whose measured amplitude is smaller than measurement uncertainties.[18]

Figure 119.12(c) reveals a toroidal topology for the $\boldsymbol{B}$ field, with a shell thickness of about 400 μm. An estimate of the maximum local $|\boldsymbol{B}|$ is then 100 MG-μm/400 μm ~ 0.3 MG. For this field, the Hall parameter $\omega_{ce}\tau$ (where ω_{ce} is the electron gyrofrequency and τ is the electron–ion collision time[14,15]) is of order 1. Since thermal conductivity is proportional to $1/\left[1+(\omega_{ce}\tau)^2\right]$ (Refs. 14 and 19), it follows that field-induced inhibition of thermal transport across the plasma bubble boundary will occur.

Interestingly, this may provide insight as to why the simulations, while correctly predicting that a toroidal $\boldsymbol{B}$ field was the primary cause of the deflections, could overestimate the field and underestimate the bubble size. Thomson-scattering[20] measurements indicated that the actual electron temperature T_e was ~40% lower than the value predicted by LASNEX (450 μm away from the foil and 600 μm from the central axis of a bubble, the measured T_e was 470 eV while the predicted value was 780 eV). With the predicted plasma temperature too high, the predicted magnetic diffusivity would be too low [since it is proportional to $T^{-3/2}$ (Ref. 14)] and the predicted $\boldsymbol{B}$ field would dissipate too slowly, leading to higher field strengths, higher $\omega_{ce}\tau$, and an even more slowly decaying electron temperature. Such considerations and more detailed data/simulation comparisons will be important for advancing our basic understanding and our predictive capabilities with various codes.

The absolute experimental determination here that the fields responsible for the structure of Fig. 119.12(b) are magnetic allows us to revisit the images of Refs. 11 and 12 (showing radiographs of similar plasma bubbles on one side of the foil only) with confidence that they also reflect magnetic fields. Reference 11 shows images that represent the complete time evolution of bubble structure throughout the 1-ns laser pulse and for an additional 2 ns afterward. Those images were recorded with the same integration time (~130 ps) as used here and show the temporal evolution of the plasma bubble radius and field magnitude. In addition, a breakdown in azimuthal symmetry was observed at times slightly later than that of Fig. 119.12(b) here.

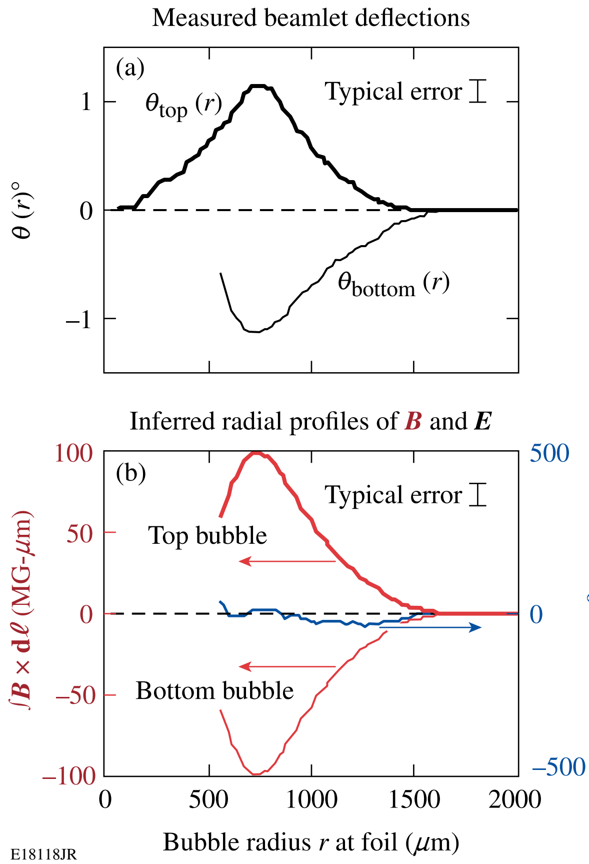

Figure 119.13
Measured beamlet deflection angles θ as a function of radius r in the top and bottom bubbles of Fig. 119.12(b) (positive is away from the bubble center), and inferred radial profiles of $\int \boldsymbol{B} \times \mathbf{d}\boldsymbol{\ell}$ and $\int \boldsymbol{E}_{\parallel} \times \mathbf{d}\boldsymbol{\ell}$ in the two bubbles. In (b), the vector $\int \boldsymbol{B} \times \mathbf{d}\boldsymbol{\ell}$ is plotted as a positive number for a toroidal $\boldsymbol{B}$ field in the clockwise direction of Fig. 119.12(c), while $\int \boldsymbol{E}_{\parallel} \times \mathbf{d}\boldsymbol{\ell}$ is plotted as positive for an $\boldsymbol{E}$ field pointing away from the bubble center. $\boldsymbol{B}$ has opposite directions in the two bubbles, while $\boldsymbol{E}$ has the same direction. Note that the absence of information about θ_{bottom} for $r <$ ~500 μm reflects the overlap of beamlets in the center of the bottom bubble image in Fig. 119.12(b), which prevented beamlet deflection measurements in that region.

Essential to the successful implementation of the technique of field discrimination and quantification are the isotropic and monoenergetic characteristics of the protons (the velocity uncertainty was <1% over the imaged plasma). Other recent important methods of ion generation from intense laser–plasma interactions,[21–23] while useful in different radiographic settings, would be compromised in the present context because of the energy spread and anisotropy of the ion fluences. In addition, other techniques of single-point field measurement at extremely high laser intensities (~10^{20} W/cm^2, Ref. 24) do not generate global field maps that show the entire laser–plasma morphology, a prerequisite to understanding plasma dynamics.

Variations of this monoenergetic proton radiography are now being applied to other important plasma/field problems in high-energy-density physics. For example, recent work in inertial confinement fusion[25,26] showed, through single-sided monoenergetic proton radiography, the presence of strong striated fields around an imploding capsule.[6] Unresolved in this work was the issue of whether the fields were magnetic or electric; yet the identification of field type is of paramount importance because different fields would involve different generation mechanisms and would have a significantly different impact on plasma evolution (through such processes as thermal transport modification). By simultaneously irradiating a subject implosion from two different directions, the methodology described above can unambiguously discern whether these fields are magnetic or electric. If magnetic, it is quite possible that the striations are a result of an electrothermal instability,[27] potentially leading to the seeding of Rayleigh–Taylor instabilities[27] that could deleteriously impact implosion dynamics.[28]

In another experiment involving accelerating, rippled plasma foils,[29] ***B*** fields are suspected—as a consequence of the Rayleigh–Taylor instability[28]—to cause the monoenergetic proton deflections seen when the foil was irradiated from a single side.[30] However, unique field and instability identification could be established by proton backlighting, from one direction, of a foil with ripples on both sides [in a fashion similar to that depicted for the two plasma bubbles in Fig. 119.12(a)]. (In such an experiment, the mesh would be removed.) In general, applying these field-mapping radiographs to a large class of high-energy-density plasmas will lead to quantifying the nature, the physical extent, and the evolution of embedded, spontaneous fields. By inference, this should also lead to new insights into the origin and dynamics of the pervasive fields of stellar jets[31] and nebulae,[32] a major goal of laboratory astrophysics.[2,33]

ACKNOWLEDGMENT

This work was supported by the Fusion Science Center (FSC) at the University of Rochester (grant no. DE-FG03-03NA00058), the National Laser Users' Facility (DE-FG52-07NA28059), the Office of Defense Programs (DE-FG52-06NA26203), Lawrence Livermore National Laboratory (subcontract Grant No. B5504974), and the Laboratory for Laser Energetics at the University of Rochester (subcontract Grant No. 412160-001G)—all through the U.S. Department of Energy. J.R.R. also acknowledges the FSC for his postdoctoral appointment. In addition, the authors express their gratitude to General Atomics and the Laboratory for Laser Energetics (LLE) for target fabrication and to LLE's laser operations team.

REFERENCES

1. W. Baumjohann and R. A. Treumann, *Basic Space Plasma Physics* (Imperial College Press, London, 1996).
2. B. A. Remington *et al*., Science **284**, 1488 (1999).
3. E. N. Parker, Astrophys. J. **128**, 664 (1958).
4. R. P. Drake, *High-Energy-Density Physics: Fundamentals, Inertial Fusion, and Experimental Astrophysics*, Shock Wave and High Pressure Phenomena (Springer, Berlin, 2006).
5. W. L. Kruer, *The Physics of Laser Plasma Interactions*, Frontiers in Physics (Westview Press, Boulder, CO, 2003).
6. J. R. Rygg, F. H. Séguin, C. K. Li, J. A. Frenje, M. J.-E. Manuel, R. D. Petrasso, R. Betti, J. A. Delettrez, O. V. Gotchev, J. P. Knauer, D. D. Meyerhofer, F. J. Marshall, C. Stoeckl, and W. Theobald, Science **319**, 1223 (2008).
7. J. M. Soures, R. L. McCrory, C. P. Verdon, A. Babushkin, R. E. Bahr, T. R. Boehly, R. Boni, D. K. Bradley, D. L. Brown, R. S. Craxton, J. A. Delettrez, W. R. Donaldson, R. Epstein, P. A. Jaanimagi, S. D. Jacobs, K. Kearney, R. L. Keck, J. H. Kelly, T. J. Kessler, R. L. Kremens, J. P. Knauer, S. A. Kumpan, S. A. Letzring, D. J. Lonobile, S. J. Loucks, L. D. Lund, F. J. Marshall, P. W. McKenty, D. D. Meyerhofer, S. F. B. Morse, A. Okishev, S. Papernov, G. Pien, W. Seka, R. Short, M. J. Shoup III, M. Skeldon, S. Skupsky, A. W. Schmid, D. J. Smith, S. Swales, M. Wittman, and B. Yaakobi, Phys. Plasmas **3**, 2108 (1996).
8. F. H. Séguin, J. A. Frenje, C. K. Li, D. G. Hicks, S. Kurebayashi, J. R. Rygg, B.-E. Schwartz, R. D. Petrasso, S. Roberts, J. M. Soures, D. D. Meyerhofer, T. C. Sangster, J. P. Knauer, C. Sorce, V. Yu. Glebov, C. Stoeckl, T. W. Phillips, R. J. Leeper, K. Fletcher, and S. Padalino, Rev. Sci. Instrum. **74**, 975 (2003).
9. F. H. Séguin, J. L. DeCiantis, J. A. Frenje, C. K. Li, J. R. Rygg, C. D. Chen, R. D. Petrasso, J. A. Delettrez, S. P. Regan, V. A. Smalyuk, V. Yu. Glebov, J. P. Knauer, F. J. Marshall, D. D. Meyerhofer, S. Roberts, T. C. Sangster, C. Stoeckl, K. Mikaelian, H. S. Park, H. F. Robey, and R. E. Tipton, Phys. Plasmas **13**, 082704 (2006).
10. J. A. Frenje, C. K. Li, F. H. Séguin, J. Deciantis, S. Kurebayashi, J. R. Rygg, R. D. Petrasso, J. Delettrez, V. Yu. Glebov, C. Stoeckl, F. J. Marshall, D. D. Meyerhofer, T. C. Sangster, V. A. Smalyuk, and J. M. Soures, Phys. Plasmas **11**, 2798 (2004).
11. C. K. Li, F. H. Séguin, J. A. Frenje, J. R. Rygg, R. D. Petrasso, R. P. J. Town, P. A. Amendt, S. P. Hatchett, O. L. Landen, A. J. Mackinnon, P. K. Patel, M. Tabak, J. P. Knauer, T. C. Sangster, and V. A. Smalyuk, Phys. Rev. Lett. **99**, 015001 (2007).
12. C. K. Li, F. H. Séguin, J. A. Frenje, J. R. Rygg, R. D. Petrasso, R. P. J. Town, O. L. Landen, J. P. Knauer, and V. A. Smalyuk, Phys. Rev. Lett. **99**, 055001 (2007).

13. G. B. Zimmerman and W. L. Kruer, Comments Plasma Phys. Control. Fusion **2**, 51 (1975).

14. S. I. Braginskii, in *Reviews of Plasma Physics*, edited by Acad. M. A. Leontovich (Consultants Bureau, New York, 1965), Vol. 1.

15. M. G. Haines, Phys. Rev. Lett. **47**, 917 (1981).

16. The disagreement between experiment and LASNEX simulation appeared to be less pronounced than this in an earlier publication,[17] but that was because the simulation utilized slightly incorrect imaging system dimensions.

17. C. K. Li, F. H. Séguin, J. A. Frenje, J. R. Rygg, R. D. Petrasso, R. P. J. Town, P. A. Amendt, S. P. Hatchett, O. L. Landen, A. J. Mackinnon, P. K. Patel, V. A. Smalyuk, T. C. Sangster, and J. P. Knauer, Phys. Rev. Lett. **97**, 135003 (2006).

18. Measurement of electric fields perpendicular to the foil in a single-bubble experiment was presented in C. K. Li, F. H. Séguin, J. A. Frenje, J. R. Rygg, R. D. Petrasso, R. P. J. Town, P. A. Amendt, S. P. Hatchett, O. L. Landen, A. J. Mackinnon, P. K. Patel, V. Smalyuk, J. P. Knauer, T. C. Sangster, and C. Stoeckl, Rev. Sci. Instrum. **77**, 10E725 (2006).

19. D. S. Montgomery *et al*., Phys. Rev. Lett. **73**, 2055 (1994).

20. D. H. Froula *et al*., Rev. Sci. Instrum. **77**, 10E522 (2006).

21. B. M. Hegelich *et al*., Nature **439**, 441 (2006).

22. M. Borghesi *et al*., Phys. Rev. Lett. **81**, 112 (1998).

23. A. J. Mackinnon *et al*., Phys. Rev. Lett. **97**, 045001 (2006).

24. M. Tatarakis *et al*., Nature **415**, 280 (2002).

25. J. Nuckolls *et al*., Nature **239**, 139 (1972).

26. S. Atzeni and J. Meyer-ter-Vehn, *The Physics of Inertial Fusion: Beam Plasma Interaction, Hydrodynamics, Hot Dense Matter*, International Series of Monographs on Physics (Clarendon Press, Oxford, 2004).

27. M. G. Haines, Can. J. Phys. **64**, 912 (1986).

28. A. Nishiguchi, Jpn. J. Appl. Phys. **41**, 326 (2002).

29. V. A. Smalyuk, S. X. Hu, V. N. Goncharov, D. D. Meyerhofer, T. C. Sangster, D. Shvarts, C. Stoeckl, B. Yaakobi, J. A. Frenje, and R. D. Petrasso, Phys. Rev. Lett. **101**, 025002 (2008).

30. R. Petrasso, Bull. Am. Phys. Soc. **52**, 97 (2007).

31. P. Hartigan *et al*., Astrophys. J. **661**, 910 (2007).

32. J. J. Hester *et al*., Astrophys. J. **456**, 225 (1996).

33. D. D. Ryutov *et al*., Phys. Plasmas **8**, 1804 (2001).